AGU PUBLICATIONS

JGR

Journal of Geophysical Research: Oceans

RESEARCH ARTICLE

10.1002/2014JC010100

Special Section:
Early scientific results from the salinity measuring satellites Aquarius/SAC-D and SMOS

Key Points:
- Demonstrates Aquarius satellite's capability to detect Atlantic TIWs
- Characterizes salinity effects on the spatial structure of Atlantic TIWs
- Reveals salinity effect on seasonal variability of Atlantic TIWs

Supporting Information:
- Readme
- Figure S1
- Figure S2
- Figure S3
- Figure S4

Correspondence to:
T. Lee,
Tong.Lee@jpl.nasa.gov

Citation:
Lee, T., G. Lagerloef, H.-Y. Kao, M. J. McPhaden, J. Willis, and M. M. Gierach (2014), The influence of salinity on tropical Atlantic instability waves, *J. Geophys. Res. Oceans*, *119*, 8375–8394, doi:10.1002/2014JC010100.

Received 30 APR 2014
Accepted 10 NOV 2014
Accepted article online 13 NOV 2014
Published online 4 DEC 2014

The influence of salinity on tropical Atlantic instability waves

Tong Lee[1], Gary Lagerloef[2], Hsun-Ying Kao[2], Michael J. McPhaden[3], Joshua Willis[1], and Michelle M. Gierach[1]

[1]Jet Propulsion Laboratory, California Institute of Technology, Pasadena, California, USA, [2]Earth and Space Research, Seattle, Washington, USA, [3]NOAA/Pacific Marine Environmental Laboratory, Seattle, Washington, USA

Abstract Sea surface salinity (SSS) data derived from the Aquarius/SAC-D satellite mission are analyzed along with other satellite and in situ data to assess Aquarius' capability to detect tropical instability waves (TIWs) and eddies in the tropical Atlantic Ocean and to investigate the influence that SSS has on the variability. Aquarius data show that the magnitude of SSS anomalies associated with the Atlantic TIWs is ±0.25 practical salinity unit, which is weaker than those in the Pacific by 50%. In the central equatorial Atlantic, SSS contribution to the mean meridional density gradient is similar to sea surface temperature (SST) contribution. Consequently, SSS is important to TIW-related surface density anomalies and perturbation potential energy (PPE). In this region, SSS influences surface PPE significantly through the direct effect and the indirect effect associated with SSS-SST covariability. Ignoring SSS effects would underestimate TIW-related PPE by approximately three times in the surface layer. SSS also regulates the seasonality of the TIWs. The boreal-spring peak of the PPE due to SSS leads that due to SST by about one month. Therefore, SSS not only affects the spatial structure, but the seasonal variability of the TIWs in the equatorial Atlantic. In the northeast Atlantic near the Amazon outflow and the North Brazil Current retroflection region and in the southeast Atlantic near the Congo River outflow, SSS accounts for 80–90% of the contribution to mean meridional density gradient. Not accounting for SSS effect would underestimate surface PPE in these regions by a factor of 10 and 4, respectively.

1. Introduction

Thousand kilometer zonal scale propagating waves with typical periods of tens of days have been observed in the tropical Pacific and Atlantic Oceans, affecting the physical and biogeochemical properties of the ocean and its interaction with the atmosphere [e.g., *Legeckis*, 1977; *Legeckis and Reverdin*, 1983; *McPhaden et al.*, 1984; *Hayes et al.*, 1989; *Luther and Johnson*, 1990; *Yoder et al.*, 1994; *Qiao and Weisberg*, 1995; *McPhaden*, 1996; *Xie et al.*, 1998; *Chelton et al.*, 2000; *Liu et al.*, 2000; *Polito et al.*, 2001; *Lee et al.*, 2012]. These tropical instability waves (TIWs) are generated from barotropic and baroclinic instabilities associated with the horizontal and vertical shear of equatorial current systems and related density gradients [e.g., *Philander*, 1978; *Weisberg and Weingartner*, 1988; *McCreary and Yu*, 1992; *Masina et al.*, 1999; *Grodsky et al.*, 2005; *Jochum et al.*, 2004; *Lyman et al.*, 2007; *von Schuckmann et al.*, 2008]. The magnitudes of TIW-related variability as seen from different oceanic parameters exhibits regional and temporal variations, varying on seasonal to interannual time scales in association with changes in the equatorial current systems. They are more energetic north of the equator because of the stronger shear of equatorial currents and the associated density gradients in the northern edge of the cold tongues in both basins [e.g., *Chelton et al.*, 2000]. They are also stronger and last longer in the Pacific than the Atlantic Ocean due to the stronger equatorial current shear and density gradients in the Pacific [e.g., *Chelton et al.*, 2000]. TIWs are important to ocean dynamics such as eddy-mean flow interaction and mixed-layer processes [e.g., *Baturin and Niiler*, 1997; *Grodsky et al.*, 2005; *Jochum and Murtugudde*, 2006; *Menkes et al.*, 2006; *Kim et al.*, 2007], ocean-atmosphere interactions [*Hayes et al.*, 1989; *Xie et al.*, 1998; *Liu et al.*, 2000; *Chelton et al.*, 2001; *Yu and Liu*, 2003; *Pezzi et al.*, 2004], and marine biogeochemistry [e.g., *Feely et al.*, 1994; *Strutton et al.*, 2001; *McCain et al.*, 2002; *Gorgues et al.*, 2005; *Evans et al.*, 2009].

TIWs are among the suite of waves in the equatorial regions, including Kelvin Waves and equatorial Rossby waves that affect ocean-atmosphere coupling. *Polito and Liu* [2003], *Farrar* [2008], *Farrar and Durland* [2012]

discussed TIWs in the context of equatorial waves in wavenumber and frequency space. While equatorial Rossby and Kelvin waves affect large-scale ocean-atmosphere coupling associated with El Niño-Southern Oscillation through the effect of basin-scale zonal SST gradient on the Walker Circulation, TIWs also affect smaller-scale air-sea interaction to regulate the tropical climate variability. In particular, TIW-related SST anomalies influence the (vertical) turbulent mixing in the marine atmospheric boundary layer, causing anomalies in ocean surface wind stress and wind stress curl that propagate westward in association with the downwind and crosswind SST anomalies of the TIWs [e.g., *Liu et al*., 2000; *Chelton et al*., 2001; *Polito et al*., 2001; *Hashizume et al*., 2001; *Chelton*, 2005].

Until recently, studies of the physical properties of TIWs have focused on satellite measurements of sea surface temperature (SST), sea surface height (SSH), ocean surface wind, and ocean color as well as sparse in situ mooring observations of temperature, salinity, and currents. The recent advances in sea surface salinity (SSS) remote sensing such as the Aquarius/SAC-D satellite mission [*Lagerloef et al*., 2008] and the Soil Moisture and Ocean Salinity (SMOS) Mission [*Boutin et al*., 2012] have provided a significant new capability to enhance our knowledge of the TIWs. Aquarius, launched in June 2011, has been providing SSS measurements since September 2011 with 7 day global coverage. *Lee et al*. [2012] demonstrated the advantage of Aquarius' SSS in improving the understanding of Pacific TIWs. In particular, Aquarius SSS data captured the dominant 17 day TIWs near the equator that were not well observed by SST and SSH. These waves traveled nearly twice as fast as the dominant 33 day TIWs away from the equator (that were well captured by SST and SSH). The improved detection of the 17 day waves was due to the fact that the meridional gradient of SSS is relatively strong while that of SST is relatively weak near the equator. The magnitude of the SSS signals associated with TIWs in the Pacific (approximately $\pm$ 0.5 practical salinity unit, or psu) is significantly larger than the target accuracy of the Aquarius mission (0.2 psu over the time scale of a month and spatial scale of 150 km). As mentioned earlier, TIWs in the Atlantic are generally weaker than those in the Pacific. There has been no systematic assessment of Aquarius' capability to study Atlantic TIWs. The motivation of this study is to perform such an assessment.

Many studies in the past of TIW energetics [e.g., *Weisberg and Weingartner*, 1988; *Qiao and Weisberg*, 1998; *Jochum et al*., 2004] did not take into account the effect of salinity on energy transfer between the mean flow and TIWs. However, significant salinity fluctuations have been observed that could regulate the baroclinic energy transfer between the mean flow and TIWs [*McPhaden et al*., 1984]. In particular, precipitation associated with the Inter-Tropical Convergence Zone (ITCZ) affects the seasonal (and conceivably interannual) variation of the horizontal gradient of SSS (and thus surface density) [*Dessier and Donguy*, 1994]. Moreover, the timing of the precipitation effect on the SSS gradient could be different from the timing of the variation of the SST gradient that is controlled by other processes. Therefore, it is important to quantify the temporal and spatial structure (1) of the SSS gradient associated with the mean flow, (2) of the SSS signature associated with the TIWs, and the relation between (1) and (2).

Based on limited observations collected by a mooring from the Prediction and Research Moored Array in the Atlantic (PIRATA) at 0°, 23°W, *Grodsky et al*. [2005] found that taking salinity variations into account in the mixed layer substantially increased the estimate of baroclinic energy conversion. Moreover, accounting for the salinity effect made the baroclinic conversion comparable to barotropic conversion. This may explain some of the discrepancies in previous studies about the relative roles of baroclinic and barotropic instability associated with TIW. However, as we will show, the location of the *Grodsky et al*. [2005] study at 0°, 23°W is actually not in the region where TIWs are the strongest. Nevertheless, that study motivates us to examine the contribution of salinity to TIWs over the entire equatorial Atlantic Ocean.

The main objective of this study is to assess Aquarius' capability to detect Atlantic TIWs and to examine the effect of SSS on Atlantic TIWs. Specifically, we investigate two aspects of SSS variability in contrast to those of SST: (1) the effect on the mean horizontal gradient of surface density and (2) the effect on the TIW-related surface density anomaly and PPE. The former has a significant implication to the latter since baroclinic instability tries to flatten the horizontal density gradient and thus convert the background available potential energy to TIW-related PPE [e.g., *Grodsky et al*., 2005]. The readers are referred to the Appendix A for a mathematical description of the energy budget associated with TIWs, how SSS affects TIW energetics, and the motivation and rationale of focusing on background density gradient, density anomalies, and PPE in our analysis. In this study, we also examine the spatial and seasonal variability of the TIWs in relation to SSS.

Most existing studies of Atlantic TIWs focused on TIW characteristics in the central equatorial Atlantic where the waves are most energetic. While that is also the main focus of this study, we also broaden the scope to examine the variability on TIW time scales in the northwestern equatorial Atlantic in relation to the Amazon plume and the North Brazil Current (NBC) retroflection into the North Equatorial Countercurrent (NECC) as well as in the southeastern Atlantic near the Congo River outflow in the southern edge of the South Equatorial Current (SEC). Variability in these regions is not associated with TIWs in the traditional sense, but it does involve the instability of the flow field such as the variability associated with the retroflected NBC and the NECC. The variability of the currents in this region is often discussed in the context of eddies and rings [e.g., *Johns et al*., 1990; *Johns et al*., 1998; *Castelão and Johns*, 2011]. Whether the variability in the northeast and southwest Atlantic are better described as eddies or Rossby waves [e.g., *Polito and Sato*, 2003] are beyond the scope of this study. Here we focus on the relation of the SSS variability in these regions to river discharges and the influence of SSS on TIWs.

In the next section, the satellite and in situ data products used in our analysis are described. Section 3 presents the results of the analysis. In section 3.1, we compare the time-mean spatial structure of SSS and the corresponding salinity gradients from Aquarius and Argo-derived products, with an emphasis on meridional gradients since they are the dominant component of the horizontal density gradient. This is followed by an investigation of the time-mean SSS and SST structure and their contributions to the meridional gradient of surface density. The analysis of the mean meridional gradient of surface density is important to the interpretation of the spatial structure of TIW-related variability discussed subsequently. In section 3.2, we present our analysis of the propagating characteristics, spatial structure, and seasonality of TIWs and compare the temporal variability of Aquarius and PIRATA data. In section 3.3, we discuss the relative contributions of TIW-related SSS anomaly (SSSA) and SST anomaly (SSTA) on surface density anomalies and PPE. Our findings are summarized in section 4.

2. Data

The data products used in the present study include satellite-derived SSS, SST, and SSH as well as in situ data from Argo floats and the PIRATA array. The SSS product is a level-3 gridded product generated by the Earth and Space Research (http://esr.org) based on Version 2, level-2 Aquarius SSS data distributed by the Physical Oceanography Distributed Active Archive Center (PO.DAAC, http://podaac.jpl.nasa.gov) for the period of September 2011 to November 2013. The level-2 SSS data were mapped to a 1/3° grid using a second-degree local polynomial fit with a 150 km search diameter. Daily maps are generated with a 7 day time window, the repeat period of Aquarius. A 1.5° smoothing is applied to the data to further suppress noise. Aquarius SSS data within approximately 150 m of the coasts are subject to land contamination. The 1.5° smoothing actually masks out some of the data near the coasts that are land-contaminated. Regions near river plumes are often associated with large spatial gradient of SSS, posing a challenge to a robust gridding to produce level-3 maps. Efforts are underway by the Aquarius project to improve the level-3 gridding algorithm. The SST product is the 1/4°, daily Optimal Interpolation Sea Surface Temperature (OISST) based on a blending of Advanced Very High Resolution Radiometer (AVHRR) and in situ SST [*Reynolds et al*., 2007, ftp://ftp.nodc.noaa.gov/pub/data.nodc/ghrsst/L4/GLOB/NCDC/AVHRR_OI). The SSH product is the 1/3°, daily maps of SSH from AVISO (http://www.aviso.oceanobs.com/) that merged data from all available altimeters.

The Argo products are the 1°, monthly gridded maps from the Asia-Pacific Data-Research Center (APDRC) of the International Pacific Research Center (IPRC) (http://apdrc.soest.hawaii.edu/projects/Argo/daa/gridded/On_standard_levels/) and from the Scripps Institution of Oceanography (SIO) (http://www.argo.ucsd.edu/Gridded_fields.html). The shallowest depth sampled by most Argo floats is 5 m. The 5 m Argo salinity (referred to as Argo SSS hereafter) is used for comparison with Aquarius SSS, which measures the upper 1 cm of the ocean. Some of the differences between the 5 m salinity measured by Argo and SSS measured by satellites, such as Aquarius and the European Space Agency's Soil Moisture and Ocean Salinity (SMOS) mission, might be related to actual near surface stratification of salinity [e.g., *Boutin et al*., 2013]. The PIRATA [*Bourlès et al*., 2008] data were obtained from the Pacific Marine and Environmental Laboratory (PMEL) of the National Oceanic and Atmospheric Administration (NOAA), http://www.pmel.noaa.gov/tao/data_deliv/deliv.html. The salinity measurements at 1 m depth (the shallowest depth sampled by PIRATA) were used

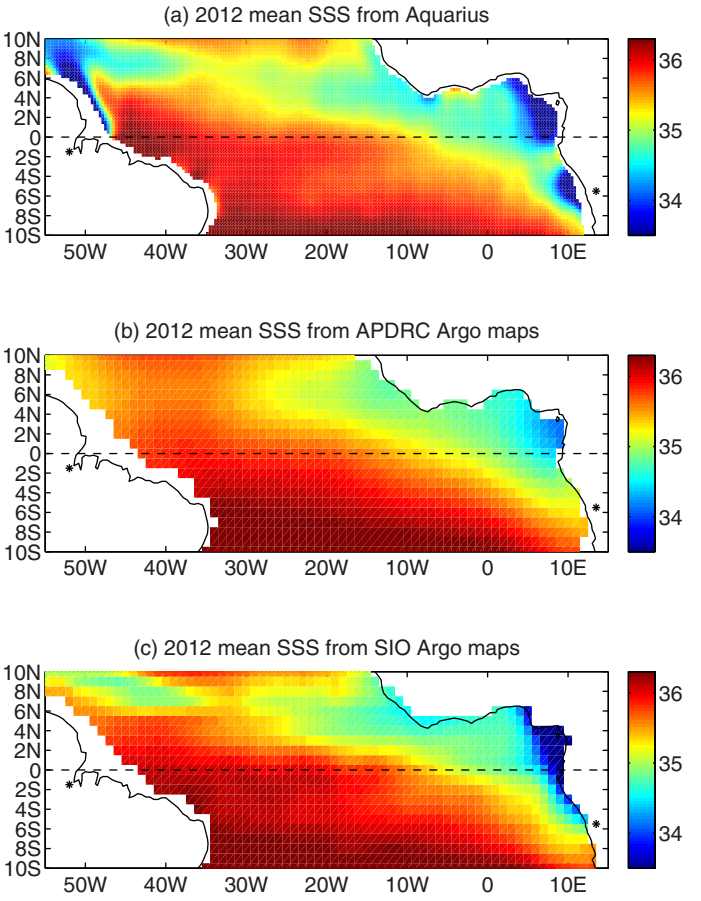

Figure 1. Annual mean SSS for 2012 from (a) Aquarius, (b) APDRC Argo product, and (c) SIO Argo product. The unit is psu. The asterisks in the west and east mark the locations near the exits of the Amazon and Congo Rivers into the Atlantic Ocean (same for all spatial maps in the rest of the paper).

for comparison with Aquarius SSS. Hereafter, the 1 m PIRATA salinity measurements are referred to as PIRATA SSS. Here we focus on the mooring data at 0° N, 23°W that has a near continuous record during the Aquarius period. This also facilitates the comparison with the finding by *Grodsky et al*. [2005] who used the mooring data at this location to study the TIWs.

3. Results

3.1. Time-Mean SSS Structure and Contribution to Density Gradient

Salinity affects TIWs by influencing the background density and regulating the TIW variability. Before discussing these waves, we describe the effect of salinity on the mean meridional density gradient, which supplies mean available potential energy to PPE through baroclinic conversion (see the Appendix A). Meridional gradient is more relevant to the predominantly zonal propagation of the TIWs than zonal gradient [*Chelton et al*., 2000]. However, there are coastal regions such as that near Brazil in the west and the Gulf of Guinea in the east where nonmeridional gradient is also important to the regional processes. We will not discuss these coastal processes in this study in order to keep the focus on the open ocean variability.

Figure 1 compares the 2012 annual mean SSS from the Aquarius, the APDRC, and the SIO Argo products for the equatorial Atlantic. The comparison is performed for 2012 only because the monthly gridded Argo maps from SIO (based on the delayed mode Argo data) only reached January 2013 at the time of our study. The spatial structure of annual mean SSS from Aquarius (Figure 1a) is qualitatively similar to that from the Argo products (Figures 1b and 1c) in terms of the overall southeast-northwest orientation of the mean SSS gradients. However, Aquarius SSS shows a much finer structure than the Argo products (especially the APDRC product). For example, the freshening effect of the ITCZ in the northern equatorial Atlantic is much sharper in Aquarius than in Argo. Moreover, Aquarius is able to capture smaller-scale features in several regions: (1) the high-salinity water carried by the NBC in the northwest, (2) the low-salinity water associated with the Amazon outflow and the NBC retroflection into the NECC, and (3) the low salinity water near the Congo River outflow in the southeast. The tongue of lower salinity water extending westward from the latitude of the Congo River outflow (near 5°S) along the southern edge of the SEC is clearly shown in the Aquarius data but is not captured by the APDRC Argo product. It is however evident in the SIO Argo product to some extent. These differences are related to the much sparser sampling by Argo floats and the relatively large smoothing scales used in generating the smooth gridded Argo maps. Argo float distribution over the global ocean is approximately one float per $3^\circ \times 3^\circ$ on average and is even coarser near the coasts, which limits the ability of Argo data to resolve the smaller-scale structure. The positions of the Argo floats in 2012 (supporting information Figure S1) show that there are several regions where the float density is very

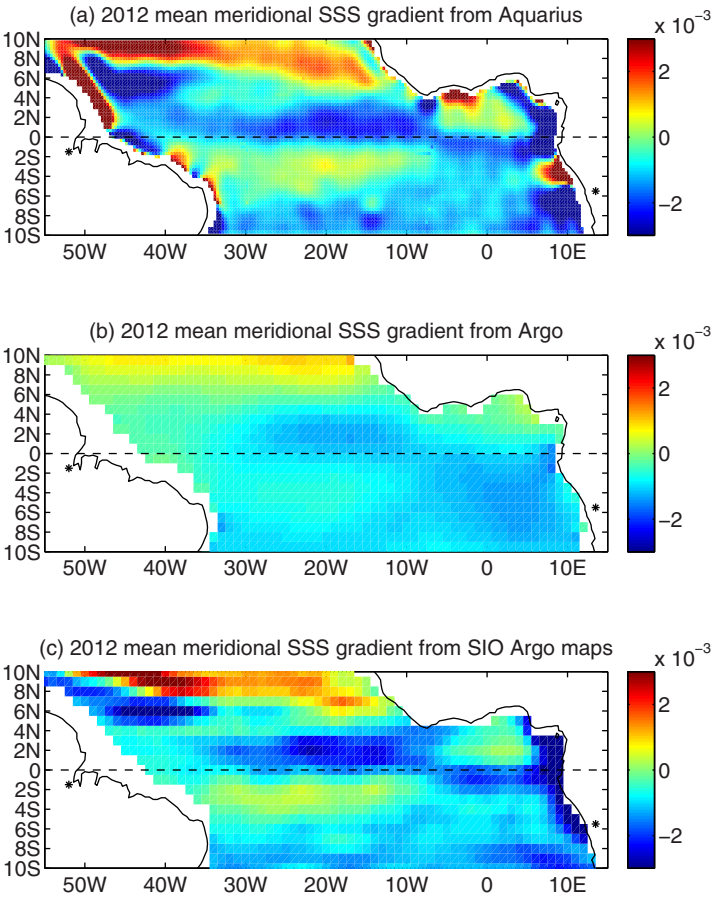

Figure 2. Annual mean meridional gradient of SSS for 2012 from (a) Aquarius, (b) APDRC Argo product, and (c) SIO Argo product. The unit is psu·km^{-1}.

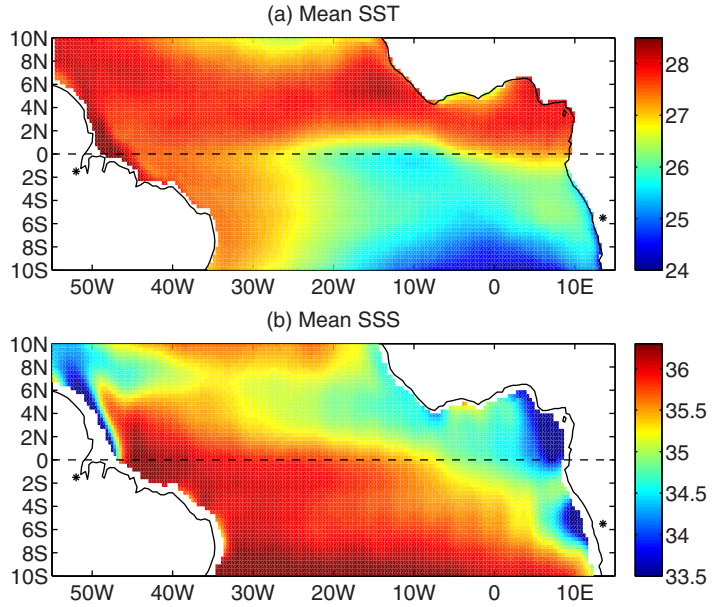

Figure 3. Temporally averaged (a) SST in °C and (b) (Aquarius) SSS in psu for September 2011 to August 2013.

low or no floats at all, such as the northwest equatorial Atlantic, eastern equatorial Atlantic between 38°W and 27°W, and southeast equatorial Atlantic. Therefore, the gridded Argo maps in these regions are subject to larger errors. While the SIO Argo product has a finer structure than the APDRC Argo product for the annual mean, it is noisier on monthly time scales.

Due to Aquarius' better spatial resolution, the Aquarius-derived meridional SSS (Figure 2a) have a much finer structure and larger gradients than those derived from Argo data (Figures 2b and 2c). Therefore, Aquarius SSS presents a significant advantage in the study of wave and eddy interaction with mean flow that involves the analysis of horizontal density gradients. Figure 3 shows the 2 year (September 2011 to August 2013) mean SST and Aquarius SSS. The time-mean SST pattern is characterized by the cold tongue extending from southeastern part toward the central equatorial Atlantic and bounded by the warmer waters to the north and west. Therefore, the meridional SST gradient is large primarily in the eastern and central equatorial Atlantic. The time-mean SSS pattern is characterized by the salty South Atlantic waters, which extend from the southeast to northwest. In the west, the meridional gradient of SST becomes much smaller while that of SSS remains relatively large.

The relative contributions of time-mean meridional gradients of SST and SSS ($\frac{\partial T}{\partial y}$ and $\frac{\partial S}{\partial y}$) to the meridional gradient of surface density ($\frac{\partial \rho}{\partial y}$) are approximated from the linear

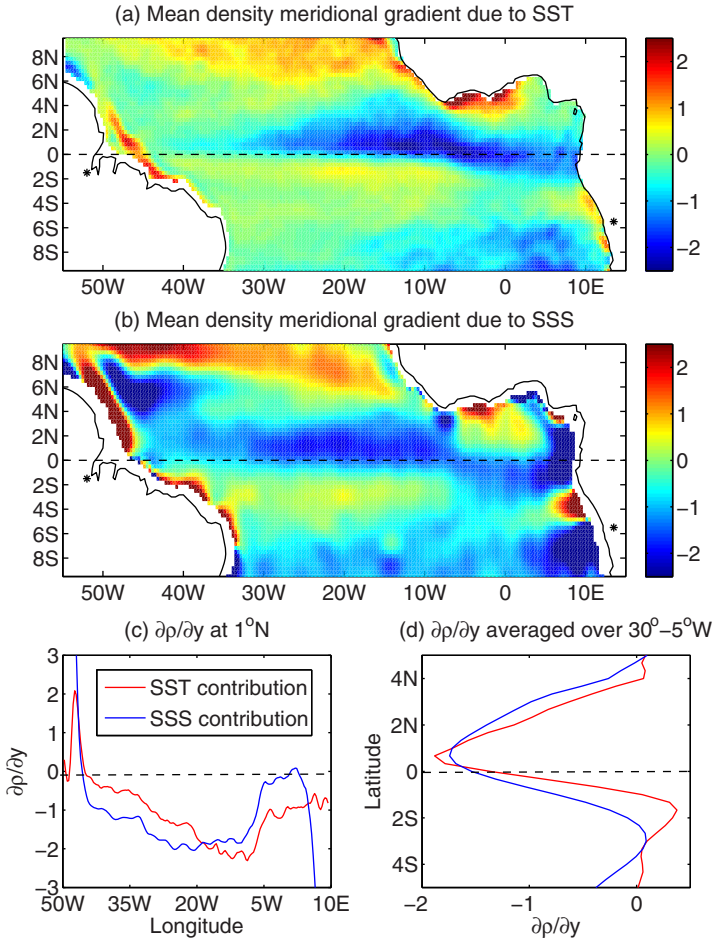

Figure 4. Time-mean meridional gradient of surface density contributed by (a) SST and (b) SSS for September 2011 to August 2013. The unit is 10^{-6} kg·m^{-4}. (c) The zonal distribution at 1°N. (d) The meridional distribution for the zonal average between 30° and 5°W.

equation of state for seawater such that $\frac{\partial\rho(T)}{\partial y} = -\alpha\rho_0 \frac{\partial T}{\partial y}$ and $\frac{\partial\rho(S)}{\partial y} = \beta\rho_0 \frac{\partial S}{\partial y}$, where α is the thermal expansion coefficient, β is the saline contraction coefficient, and ρ_0 is mean density of seawater (1025 kg·m^{-3}). At the sea surface, 26.7°C mean temperature and 35.3 psu mean salinity for the equatorial Atlantic Ocean (5°S–5°N) during the period of the study, the values of α and β are 3.11×10^{-4}°C^{-1} and 7.36×10^{-4} psu^{-1}, respectively. The resultant $\frac{\partial\rho(T)}{\partial y}$ and $\frac{\partial\rho(S)}{\partial y}$ are shown in Figure 4. The negative values of surface meridional density gradient indicate warmer and/or fresher surface waters to the north and vice versa.

In the northern equatorial Atlantic, $\frac{\partial\rho(T)}{\partial y}$ is generally larger in the eastern half while $\frac{\partial\rho(S)}{\partial y}$ is larger in the western half of the basin. The zonal distributions of $\frac{\partial\rho(T)}{\partial y}$ and $\frac{\partial\rho(S)}{\partial y}$ at 1°N where TIWs have been found to be the most energetic for SST [e.g., *Chelton et al.*, 2000; *Caltabiano et al.*, 2005] are shown in Figure 4c. In the east between 19°W and 5°E (the two crossings of the two curves), the ratio of $\frac{\partial\rho(T)}{\partial y}$ and $\frac{\partial\rho(S)}{\partial y}$ is 1.6. In the west between 47° and 19°W (the two crossings of the two curves), the ratio of $\frac{\partial\rho(S)}{\partial y}$ and $\frac{\partial\rho(T)}{\partial y}$ is 1.8. The meridional distributions of $\frac{\partial\rho(T)}{\partial y}$ and $\frac{\partial\rho(S)}{\partial y}$ averaged in the central equatorial Pacific between 30° and 5°W are presented in Figure 4d. The values of $\frac{\partial\rho(T)}{\partial y}$ and $\frac{\partial\rho(S)}{\partial y}$ are similar between 0° and 2°N, especially at 1°N where they are equal (where the two curves cross). Within 5° of the equator, the largest difference between $\frac{\partial\rho(T)}{\partial y}$ and $\frac{\partial\rho(S)}{\partial y}$ occurs at 1°S where $\frac{\partial\rho(S)}{\partial y}$ is 14 times larger than $\frac{\partial\rho(T)}{\partial y}$. In the NBC retroflection region in the northwest (47°–40°W, 4°–6°N), SSS accounts for approximately 90% of the meridional density gradient. The freshwater discharge from the Congo River in the southeast sets up positive density gradients between 2 and 4.5°S and negative density gradients south of 4.5°S to the east of 5°E. For the region near the center (4.5°–6.5°S, 5°–10°E) of the Congo River outflow, SSS accounts for 80% of the contribution of mean meridional density gradient. These features of mean meridional density gradient are helpful to understand the spatial variability of TIW characteristics and PPE as discussed in the next section.

3.2. Spatial and Temporal Signature of TIWs in SSS, SST, and SSH

Aquarius is able to capture the salinity structure of the Atlantic TIWs. The example in Figure 5 shows the spatial structure of the TIWs on 30 December 2011. In the figure, plot a shows SSS and SST; plot b shows SSS and SSHA; plot c shows SST and SSHA. Another example for 16 July 2012 is shown in Figure S4 (supporting information). The examples correspond to the season when the Amazon plume went northwestward (Figure 5a) and the season when it turned eastward along with the retroflection of the NBC (supporting information Figure S2a). The signature of TIW SST is strongest in the central part of the basin (especially between 10° and 20°W) slightly north of the equator, which is consistent with previous observations

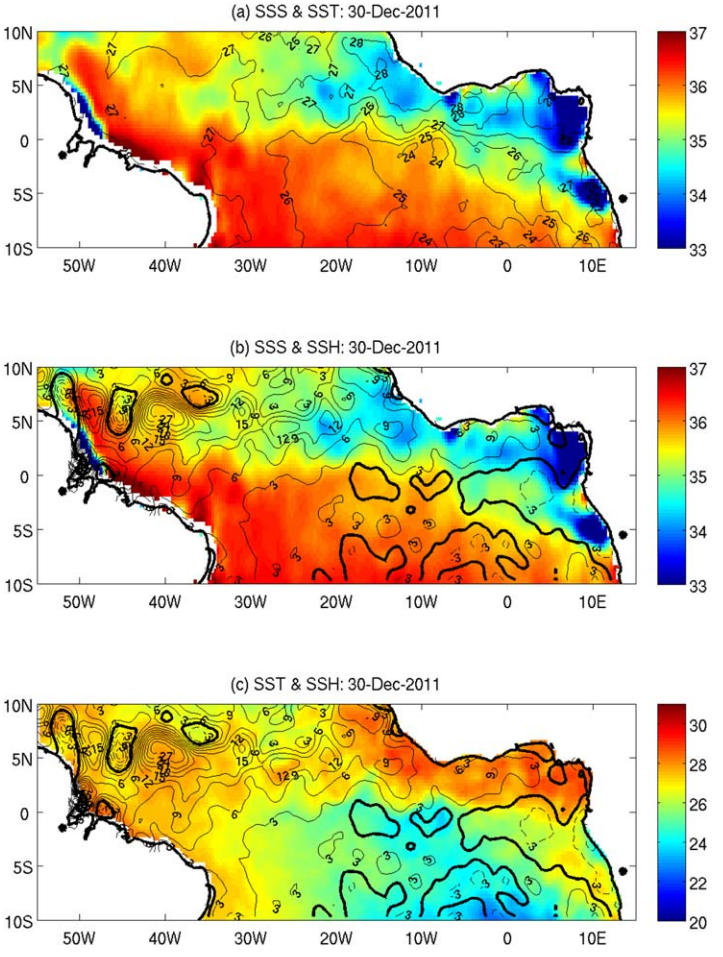

Figure 5. TIWs spatial structure on 30 December 2011 shown by SSS, SST, and SSH: (a) SSS in color shading and SST in contours. (b) SSS in color shading and SSH in contours, and (c) SST in color shading and SSH in contours. The units for SSS, SST, and SSH are psu, °C, and cm, respectively.

(e.g., by *Caltabiano et al*. [2005] based on satellite measurements of SST). While the wave structure in SST diminishes toward the west, that in SSS remains very clear in the northwest. In the central equatorial Atlantic, the wave signature in SSS, SST, and SSHA are more coherent. For example, a northward protrusion of the higher SSS is generally associated with a lower SST. Both of these correspond to a lower SSHA. This is similar to the TIW-related structure in the eastern equatorial Pacific for SSS, SST, and SSHA [e.g., *Lee et al*., 2012, Figure 1]. These coherent changes among SSS, SST, and SSHA are not seen in the northwest Atlantic near the NBC retroflection region. Figure 8b actually shows high (low) SSS associated with positive (negative) SSHA in this region. These SSHA are probably related to barotropic instability associated with the NECC [*Jochum and Malanotte-Rizzoli*, 2003] that radiate to the NBC to affect the generation of the NBC rings.

Figure 6 shows the comparison between Aquarius and PIRATA SSS at 0°, 23°W (the mooring location with the longest near continuous record during the Aquarius period) for the unfiltered values and for the filtered anomalies in the 20–50 day band. *Chelton et al*. [2000] found that the TIWs were energetic at periods shorter than 50 days. We found that the variability shorter than 20 days is very weak in the tropical Atlantic. We therefore focus on the 20–50 day band. The filter used is a second-order, zero-phase (forward-reverse) Butterworth filter. Before filtering the PIRATA time series, the short data gap in early 2013 seen in Figure 6a was filled in by linear interpolation. At this location, the time mean value of Aquarius SSS is fresher than that of PIRATA SSS by 0.03 psu. The root-mean-squared (RMS) difference between Aquarius and PIRATA SSS anomalies is 0.17 psu. The RMS difference between the respective 20–50 day filtered values is 0.08 psu. The RMS difference of 0.17 psu is smaller than the mission target accuracy of 0.2 psu over 1 month and 150 km even though the RMS difference we calculated includes time scales shorter than a month. Part of the difference seen in Figure 6 is due to the fact that the effective spatial resolution of the Aquarius maps is approximately 150 km whereas the PIRATA measurements are point-wise observations. The standard deviation of the Aquarius SSS (0.23 psu) is smaller than that of the PIRATA SSS (0.28 psu) by 17%. For the 20–50 day filtered time series, Aquarius' standard deviation (0.10 psu) is smaller than that of PIRATA (0.13 psu) by 25%. The smaller variability in Aquarius SSS is consistent with the effects of spatial averaging. The correlation between the Aquarius and PIRATA time series is 0.79 both for the unfiltered and filtered time series. The value of the correlation coefficient is significant at the 95% confidence level even if we assume that the data are independent at 7 day time scale, which is the running time window for the daily Aquarius maps. Figure S3 (supporting information) compares the unfiltered and filtered time series of salinity anomalies for Aquarius and PIRATA. The

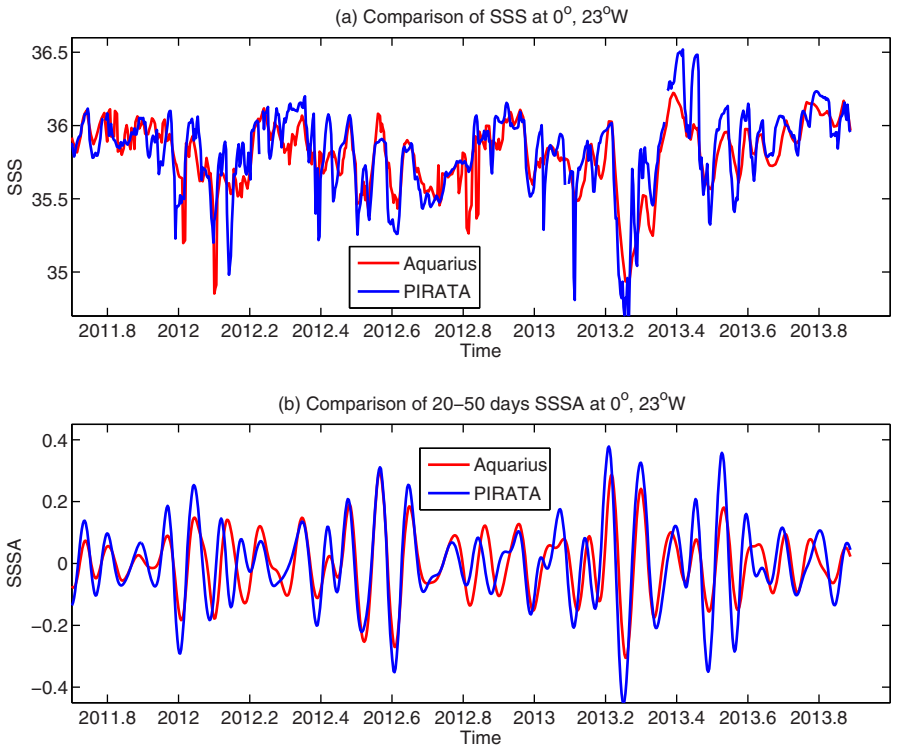

Figure 6. Comparison of Aquarius and PIRATA SSS (a) and 20–50 day filtered SSS anomalies (b) at 0°, 23°W.

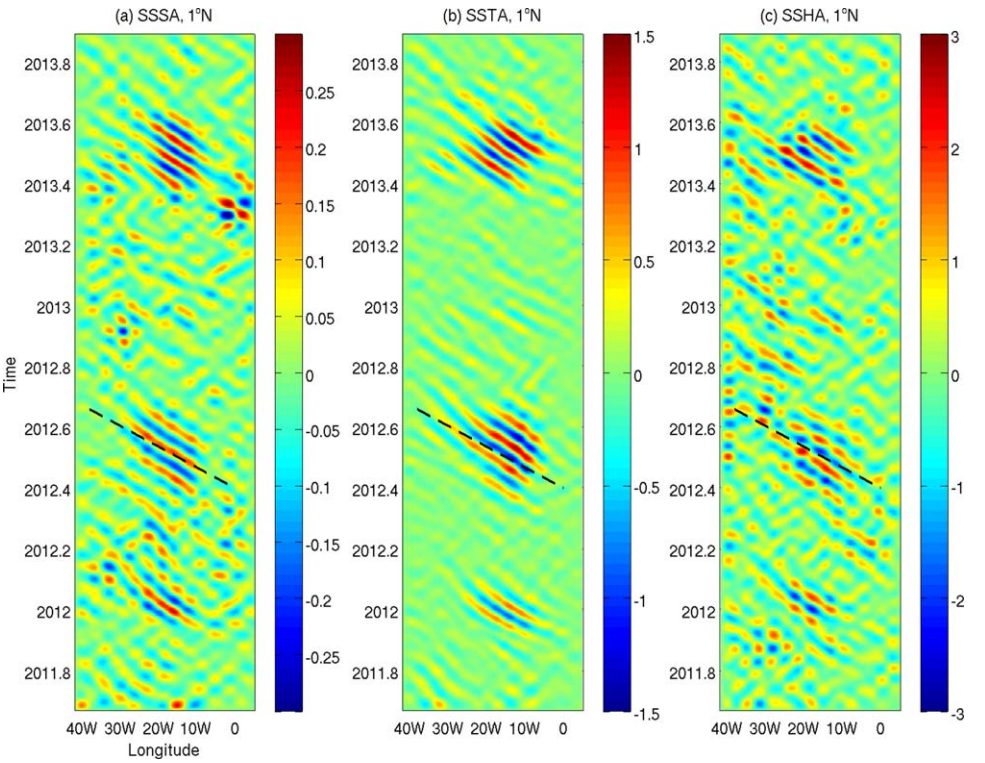

Figure 7. Longitude-time distribution of 20–50 day, 4–20° longitudinal filtered (a) SSSA, (b) SSTA, and (c) SSHA at 1°N. The units are psu, °C, and cm, respectively. The dashed lines correspond to 0.5 m·s^{-1} westward propagation speed.

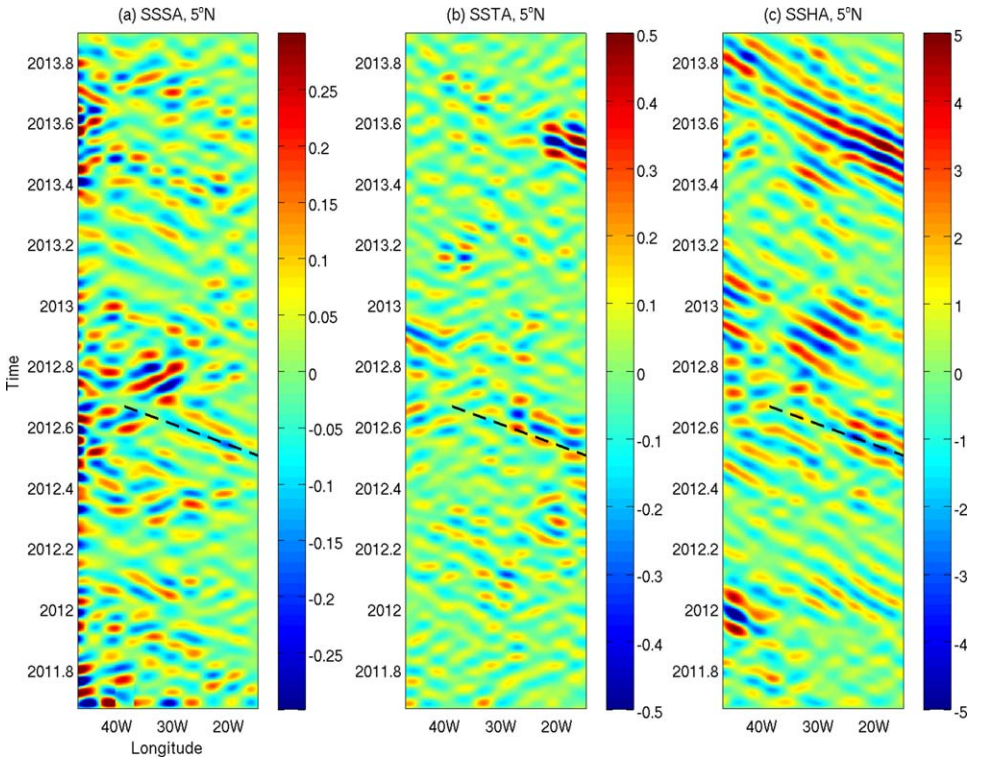

Figure 8. Longitude-time distribution 20–50 day, 4–20° longitudinal filtered (a) SSSA, (b) SSTA, and (c) SSHA at 5°N near the latitudes where the NBC retroflects into the NECC. The units are psu, °C, and cm, respectively. The dashed lines correspond to 0.5 $m \cdot s^{-1}$ reference for westward propagation speed.

variance explained by the 20–50 day filtered time series is 25% for Aquarius and 31% for PIRATA. They are statistically significant because a two-sample F-test suggests that the unfiltered and the unfiltered-minus-filtered (i.e., residual) time series do not have the same variance at 95% confidence level.

Westward propagation is evident in the SSSA, SSTA, and SSH anomaly (SSHA) data. An example is shown in Figure 7 for the longitude-time distributions of the anomalies of these variables at 1°N for the period band of 20–50 days and wavelength band of 4–20°, which encompass the most energetic TIWs in frequency and wavenumber space reported by various studies. The second-order, zero-phase Butterworth filter is used both for the temporal and spatial band-pass filtering. Westward propagation speed estimated from the Radon Transform for the data between 40°W and 5°E is 0.49, 0.51, and 0.51 $m \cdot s^{-1}$ for the SSSA, SSTA, and SSHA, respectively. The 0.5 $m \cdot s^{-1}$ westward propagation speed is depicted by the dashed line in Figure 7. This is higher than the 0.3 $m \cdot s^{-1}$ speed estimated from microwave (TMI) SST during 1998–1999 by *Chelton et al*. [2000] at the same latitude of the Atlantic Ocean for 50 day high-pass signals. Whether this difference is due to time period or due to different data sets will be investigated in the future in order to keep our focus on the role of salinity on TIW energetics. During part of the study period, slower propagation is evident in the western than the eastern part of the basin. This is the case, for instance, in early 2012 for both SSSA and SSTA.

The maximum amplitude of the SSS signals at this latitude, approximately ±0.25 psu (Figure 7a), is smaller than that of the TIWs in the Pacific between 0° and 2°N by approximately 50%. Apart from the dominant westward propagating signals, there are weaker anomalies that appear to propagate eastward. These anomalies reflect the noise in the measurements. Their magnitudes, approximately 0.05–0.1 psu for SSSA, 0.1–0.2°C for SSTA, and 0.5–1 cm for SSHA, are well within the respective measurement uncertainties.

The seasonality of the TIW-related SSTA and SSSA signatures are somewhat different. In the central part of the basin, the strongest SSSA signals occur earlier than the strongest SSTA signals by tens of days (this is illustrated more clearly in Figure 11 that will be discussed later). As explained in the next section in relation to Figure 15, this is because the timing of the peak magnitude of meridional SSS gradient occurred earlier

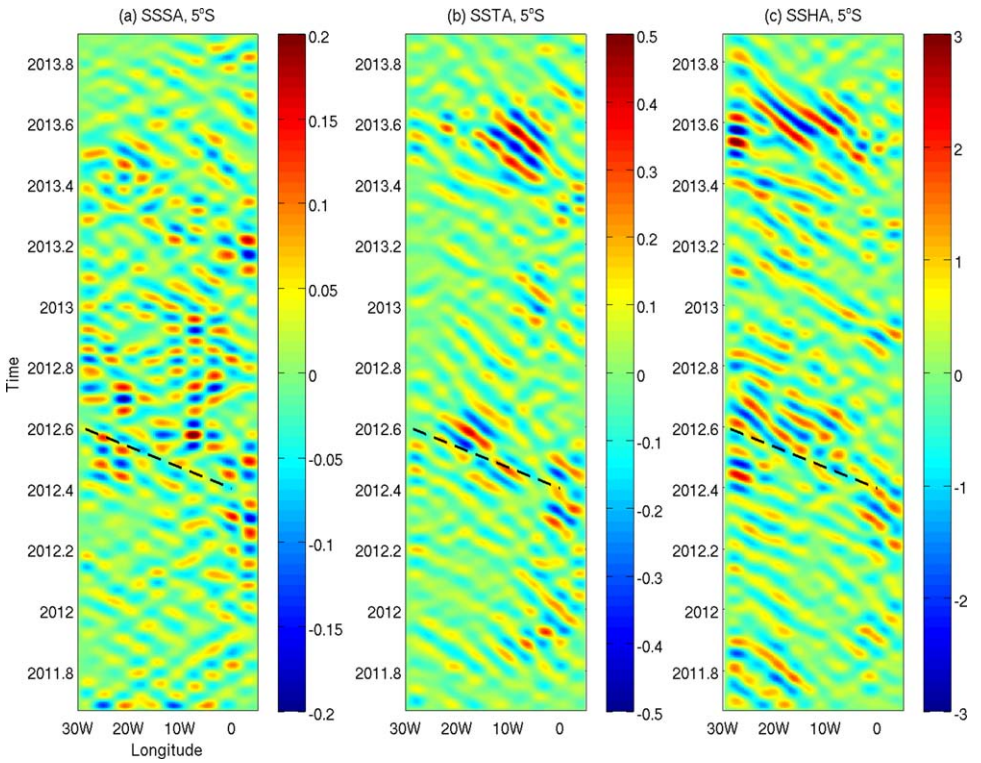

Figure 9. Longitude-time distribution of 20–50 day, 4–20° longitudinal filtered (a) SSSA, (b) SSTA, and (c) SSHA at 5°S near the latitudes of the Congo River outflow. The units are psu, °C, and cm, respectively. The dashed lines correspond to 0.5 $m \cdot s^{-1}$ reference for westward propagation speed.

than that of meridional SST gradient, so that the same TIW velocity signal affects SST and SSS perturbations differently. In terms of spatial structure, the strongest signals for all three parameters are centered near 10°–20°W at this latitude. However, the SSSA signals are somewhat more evident than the SSTA signals in the western and eastern part of the basin. This is particularly true at other latitudes (not shown) where the meridional SST gradients do not extend as far west compared to 1°N.

At 5°N (Figure 8), westward propagation is evident in all 3 variables but is the clearest in SSHA. Note that the range of the color scale for SSTA is 0.5°C in Figure 8 and 1.5°C in Figure 7, and that for SSHA is 5 cm in Figure 8 and 3 cm in Figure 7. These choices allow a better visualization of the dominant signals at 5°N and 1°N. The westward propagation speed estimated from Radon Transform for the data east of 35°W is 0.46, 0.44, and 0.46 $m \cdot s^{-1}$ for SSSA, SSTA, and SSHA, which are not statistically different. Based on the average phase speed of 0.45 $m \cdot s^{-1}$ and average frequency of 0.0035 $cycle \cdot day^{-1}$ for this band, the average wavelength and wavenumber are 1111 km and 0.0009 $cycle \cdot km^{-1}$. This frequency-wavenumber characteristics lies between the dispersion curves of the mixed Rossby-Gravity Wave (i.e., Yanai Wave) and the first-baroclinic Rossby Wave [e.g., *Polito and Sato*, 2003, Figure 3; *Farrar*, 2008, Figure 1] and close to the dispersion curve for the theoretical prediction of TIWs [*Lyman et al*., 2005, Figure 9; *Farrar*, 2008, Figure 1]. Therefore, the westward propagating waves at this latitude are more suitably described as TIWs. Based on analysis of SSH data, *Polito and Sato* [2003] showed that the first-baroclinic Rossby Waves in the northern equatorial Atlantic is energetic primarily west of 35°W with a dominant period of 63 days, phase speed of 0.33 $m \cdot s^{-1}$, and wavelength of 1622 km. These characteristics are quite different from those of the westward propagating signals shown in Figure 8. *Richardson and Reverdin* [1987] also discussed meanders associated with the retroflection of the NBC into the NECC based on in situ data.

For SSSA (Figure 8a), there appear to be eastward propagating signals in the western part of the basin starting around midyear, especially in 2012. This is the time when the retroflection of the NBC into the eastward-flowing NECC is the strongest, accompanied by the eastward intrusion of the low salinity water

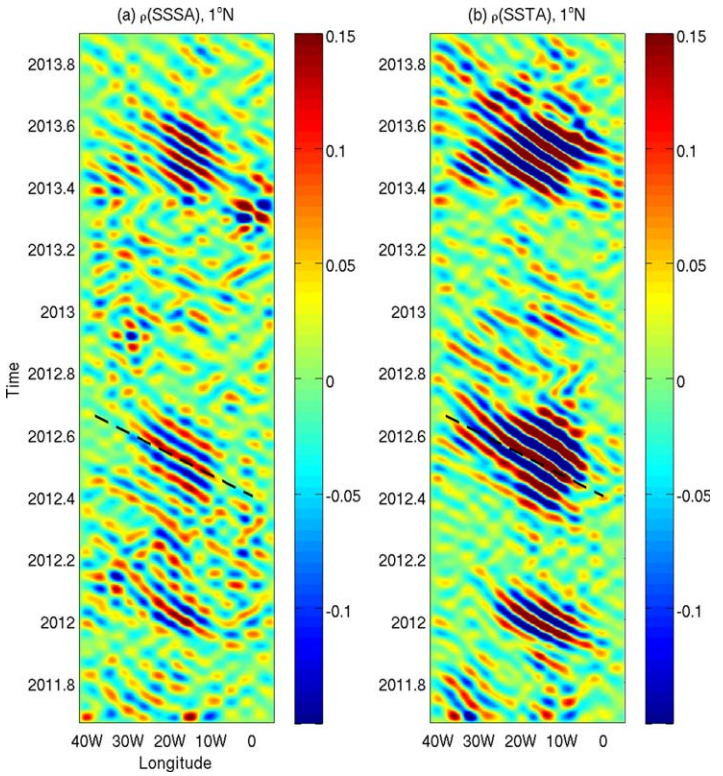

Figure 10. Longitude-time distribution of the surface density anomaly at 1°N due to 20–50 day, 4–20° longitudinal filtered (a) SSSA and (b) SSTA. The unit is kg·m^{-3}. The dashed lines correspond to 0.5 m·s^{-1} westward propagation speed.

from the Amazon plume. For SSHA (Figure 8c), the predominant westward propagating signals are disrupted in mid-year by what appears to be weaker signals of eastward propagation. However, the magnitude of the signals is within measurement errors.

The eastward propagation in SSHA at 5°N is actually identifiable in the unfiltered SSS from Aquarius (supporting information Figure S4a) as well as from the monthly Argo data (not shown). Analysis of the Aquarius data suggests that the eastward propagation tendency exists not just in the band-pass filtered data, but is relatively broad-banded, especially in longer periods and wavelengths. Examples are shown for the 20° low-pass SSS (supporting information Figure S4b) and the 4°–20° band-pass SSSA (supporting information Figure S4c). The eastward propagation tendency is likely to be related to the eastward advection by the NECC as well as by the precipitation associated with the Inter-tropical Convergence Zone (ITCZ). The time-mean eastward surface velocity at 5°N between 40° and 20°W is approximately 0.2–0.25 m·s^{-1} [*Lumpkin and Garzoli*, 2005]. But the eastward velocity of the NECC is stronger during early summer and exhibits strong interannual variation, for example, with a value of about 0.2 m·s^{-1} in July 2004 and 0.4 m·s^{-1} in July 2005 [*Urbano et al.*, 2008]. The eastward propagation speed estimated from the Aquarius data in the second half of 2012 using Radon Transform is 0.81 m·s^{-1} for the unfiltered data and 0.53 m·s^{-1} for the 4–20°, 20–50 day band-pass filtered data. While these estimates are faster than the surface speed of the NECC, they are not very robust because of the limited time period used for the estimation. In particular, the higher speed estimated from the unfiltered data is a result of some of the near zonal structure. The nature of the eastward propagating signals seen in Figure 8 and Figure S4 (supporting information) needs further investigation.

At 5°S (Figure 9) near the center latitude of the Congo River outflow and the southern edge of the SEC, there is evidence of westward propagation in SSHA and SSTA with a speed that varies in space and time. Some of the signals (e.g., in SSTA) originate from the eastern side of the basin, i.e., the Congo River outflow. Others emerge in the middle of the basin. In SSSA, westward propagating features are not as coherent and the magnitude of the anomalies is relatively small except in the eastern side near the Congo River outflow region. This is likely because the magnitude of the SSS signals related to these waves away from the Congo River outflow region is at the noise level of the Aquarius data.

3.3. Relative Contributions of SSS and SST to Surface Density and Potential Energy

The relative contributions of SSSA and SSTA to surface density anomaly at 1°N are shown in Figure 10 with $\rho_o \beta S'$ and $-\rho_o \alpha T'$ presented in plots a and b (where S' and T' are SSSA and SSTA shown in Figures 7a and 7b). The contribution by SSSA is comparable to that by SSTA in the central parts of the basin. However, SSSA generally makes larger contributions in the western and eastern part of the basin. The time series of $\rho_o \beta S'$ and $-\rho_o \alpha T'$ at (1°N, 16°W) is shown in Figure 11. The standard deviations for the two contributions

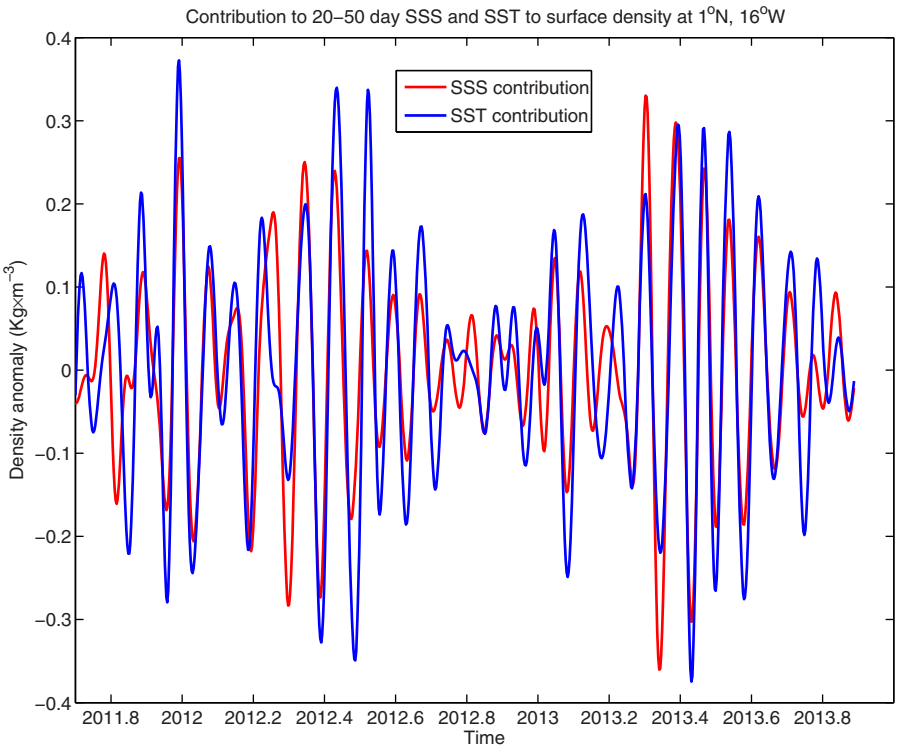

Figure 11. Contributions of 20–50 day filtered SSSA and SSTA to surface density anomaly at 1°N, 16°W.

are 0.08 and 0.09 kg·m^{-3} at this location. Overall speaking, SSSA and SSTA contributions to surface density anomaly reenforce each other because of the opposite sign of time-mean SSS and SST gradients at this location (Figure 3). Thus the same meridional current advecting these gradients (Figure 4) will produce reenforcing tendencies of density variability.

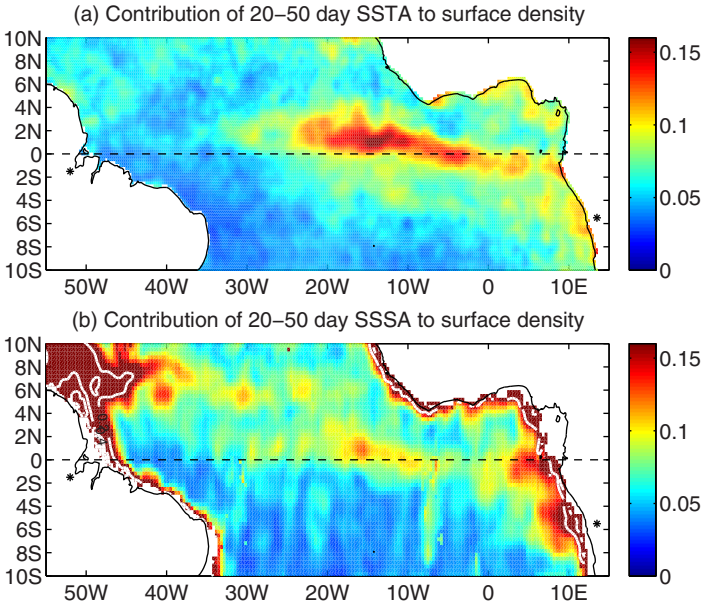

Figure 12. The standard deviation of the contribution of 20–50 day (a) SSTA and (b) SSSA to surface density anomaly. The unit is kg·m^{-3}. The upper limit of the color shading is 0.16. The large values near the coasts with a maximum up to 1.2 near the Amazon outflow are shown by contours starting from 0.2 with in increment of 0.2.

The spatial structure of the 20–50 day period SSTA and SSSA contributions to surface density anomalies (i.e., the standard deviation of the contributions of the filtered SSTA and SSSA to density anomaly) are shown in Figure 12. A band with relatively large SSTA contribution extends from approximately 23°W to the eastern boundary (Figure 12a). The maximum SSTA contribution to density anomaly occurs near (1°N, 16°W). The SSSA contribution to density anomaly is also large near this location (Figure 12b). In the equatorial zone and west of 23°W, SSSA has a larger contribution. This includes the PIRATA mooring location of (0°, 23°W) where *Grodsky et al.* [2005] performed

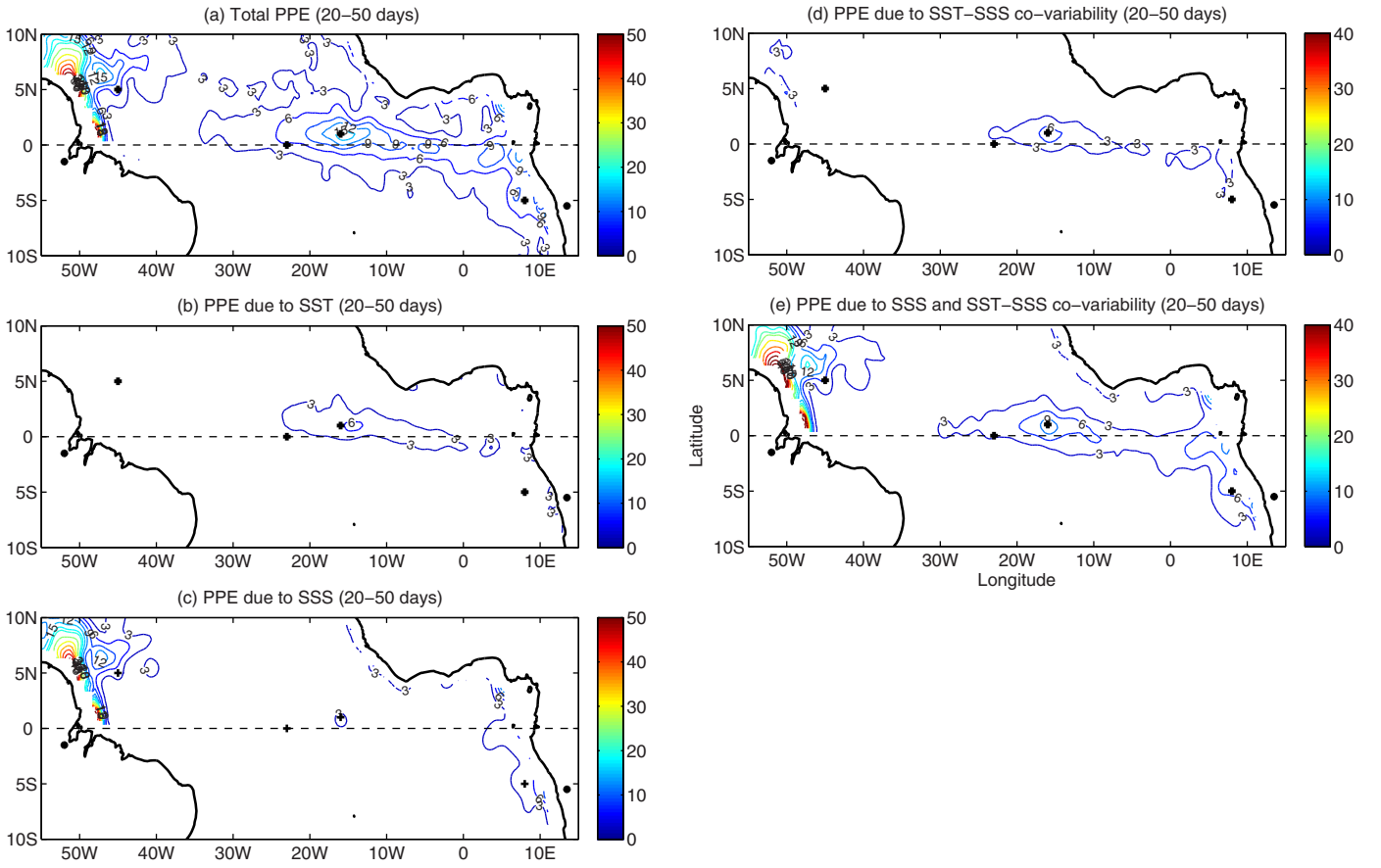

Figure 13. The time mean of the (a) total PPE, (b) direct contribution by SSTA, (c) direct contribution by SSSA, all for the 20–50 day signals. The unit is Joule·m^{-3}. The crosses correspond to locations where the PPE time series are presented in Figure 14. (d) The time mean contribution by 20–50 day signals to PPE due to SSTA-SSSA covariability and the sum (c) and (d) that reflects the combined direct and indirect effect of SSS. The unit is Joule·m^{-3}. The crosses correspond to locations where the PPE time series are presented in Figure 14.

their analysis of salinity's influence on TIWs. In the northwest near the Amazon outflow and NBC retroflection into the NECC and in the southwest near the Congo River outflow region, the surface density anomalies are almost entirely contributed by SSS.

While the contributions of SSTA and SSSA to surface density anomaly are relatively linear through the linear equation of state $\rho' = \rho_o(-\alpha T' + \beta S')$ at the sea surface, their contributions to surface PPE are not. Assuming the TIW-related SST and SSS anomalies are representative of the corresponding anomalies averaged vertically within the mixed layer, the PPE for the mixed layer (referred to as PPE for the sake of convenience hereafter) can be expressed as

$PPE = g\rho'^2/(2\rho_{oz}) = g\rho_o{}^2/2\rho_{oz}\,[(-\alpha T')^2 + (\beta S')^2 - 2\alpha\beta T'S']$ [*Weisberg and Weingartner*, 1988; *Grodsky et al*., 2005, also see equation (A(A2b)) in the Appendix A), where ρ_{oz} is the vertical gradient of mean density at the base of the mixed layer (determined from Argo data in the equatorial Atlantic). It includes the direct contribution of SSTA (the first term), SSSA (the second term), and the contribution due to the covariability of SSTA and SSSA (the third term). The sum of the second and third term indicates the effect of total contribution by salinity, i.e., the effect that would be missed if salinity were not taken into account in the analysis of PPE. PIRATA mooring data suggest that TIW-related anomalies of temperature and salinity primarily occur in the mixed layer [*Grodsky et al*., 2005]. Therefore, mixed-layer PPE is very helpful to understand the baroclinic conversion associated with TIW-mean flow interaction.

Figure 13 shows the 2 year (September 2011 to August 2013) mean of the total PPE, direct contribution by SSTA, SSSA, and SSTA-SSSA covariability, and the sum of the latter two, all for the 20–50 day signals. Within 2–3° of the equator, large PPE is seen in the central equatorial Atlantic between 25°W and 0°E north of the equator and east of 0°E south of the equator. This pattern resembles that of the mean meridional density

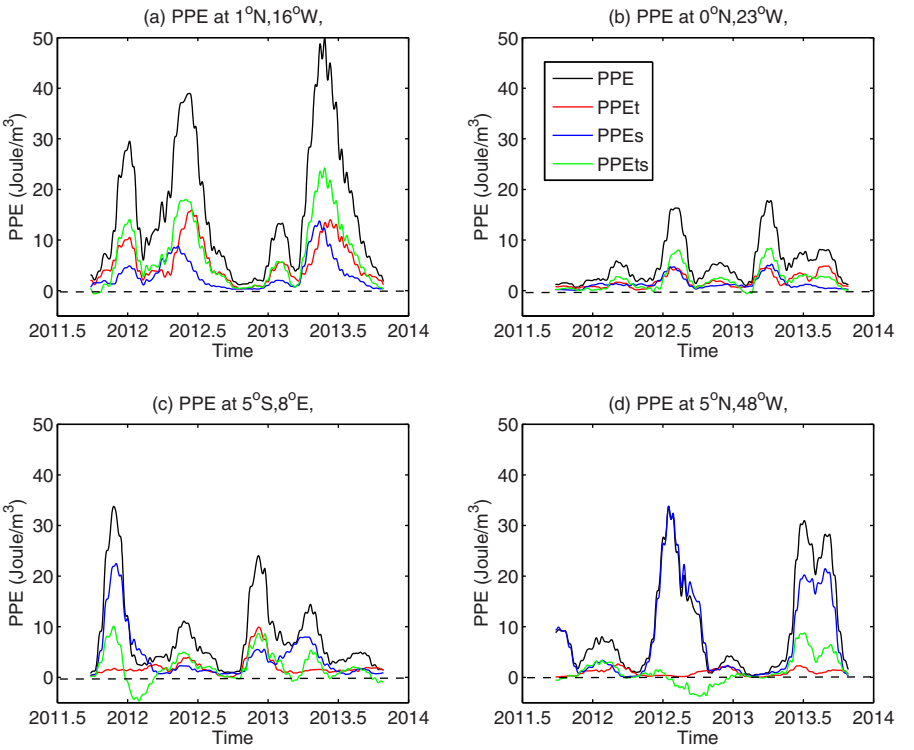

Figure 14. Time series of 50 day running average of PPE and the contributions by SST only, SSS only, and by SST-SSS covariability at the four locations marked by the white crosses in Figure 13. The legends for the curves are the same for different plots.

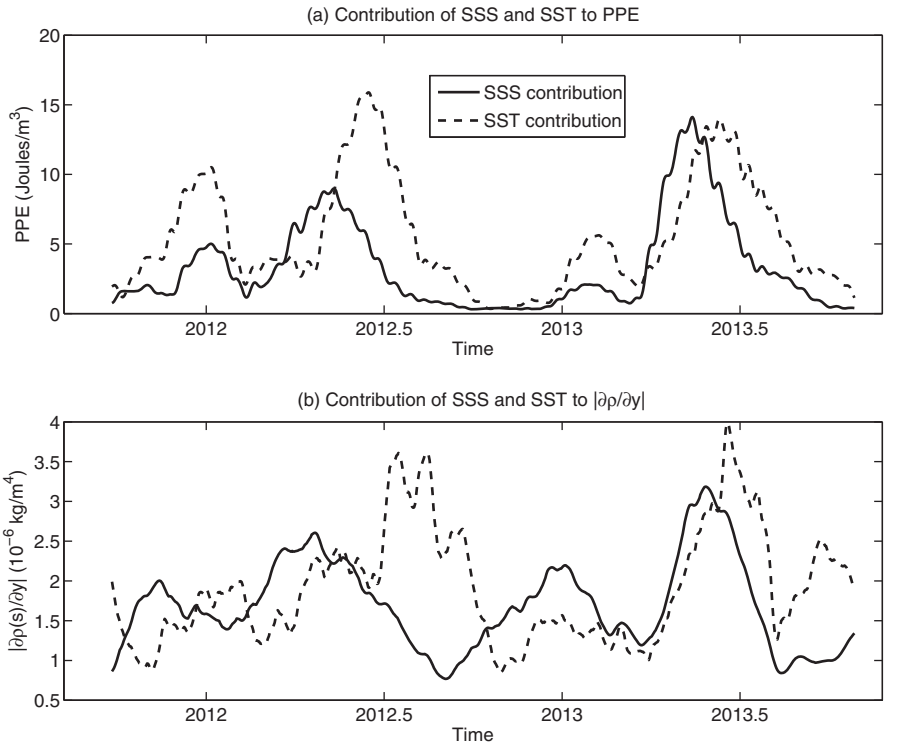

Figure 15. Contribution of SSS and SST to (a) PPE and (b) meridional density gradient at 1°N, 16°W. The legends for the curves are the same for two plots.

Table 1. Time-mean PPE and the Contributions by SST, SSS, SST-SSS Covariability Obtained From the Time Series Presented in Figure 14 are Listed in Columns 2–5[a]

	PPE	PPEt	PPEs	PPEts	PPEs+PPEts	PPE/PPEt
1°N, 16°W	15.8	5.5	3.3	7.0	10.3	2.9
0°, 23°W	5.4	1.9	1.4	2.1	3.5	2.9
5°S, 8°E	8.1	2.1	4.0	2.0	6.0	4.0
5°N, 48°W	9.8	0.9	7.7	1.1	8.9	10.4

[a]The sum of the later two is provided in column 6. The ratio between total PPE and the SST contribution is provided in column 7.

gradient shown in Figure 2a). In addition, large PPE is found in the NBC retroflection region in the northwest and the Congo River outflow region in the southeast (Figure 13a). The direct contribution of SSTA to PPE (Figure 13b) is largest in the equatorial zone. The direct contribution of SSSA to PPE (Figure 13c) and the contribution of SSTA-SSSA covariability to PPE (Figure 13d) both have a local maximum in the central-north equatorial Atlantic between 0 and 2.5°N and between 23°W and 10°W. The positive contribution by the SSTA-SSSA covariability in the central equatorial Atlantic is because the perturbation of the mean meridional gradients of SST and SSS (Figures 3a and 3b) by TIW-related meridional velocity generally results in positive SSTA and negative SSSA, and vice versa. Figure 13 also suggests that the PPE near the NBC retroflection and the Congo River outflow regions are primarily contributed by SSSA.

To examine the seasonality of the PPE and the contributions of SSTA and SSSA to it, we present in Figure 14 the time series of the 50 day running mean of PPE and the contributions by SST only, SSS only, and SST-SSS covariability for the four locations masked by the white crosses in Figure 13. They include (a) 1°N, 16°W (where the PPE is the largest), (b) a PIRATA mooring location at 0°, 23°W where *Grodsky et al.* [2005] found a substantial role of salinity in baroclinic energy conversion rate (i.e., the conversion of background available potential energy to the PPE), (c) 5°S, 8°E near the Congo River outflow, and (d) 5°N, 48°W near the NBC retroflection. The time-mean values of PPE and the contributions SST, SSS, SST-SSS covariability from these time series are listed in Table 1, denoted by PPE, PPEt, PPEs, and PPEts. The value of PPEs+PPEEts, reflecting total contribution by SSS, and the ratio between PPE and PPEt, indicating how many times PPE would be underestimated if SSS effects are ignored, are also listed in the table.

At 1°N, 16°W, the largest contribution to PPE comes from PPEts, followed by PPEt and PPEs (Table 1). Considering only the SST contribution, i.e., ignoring the direct and indirect effects of SSS, would underestimate the PPE by almost three times. The seasonal peak of the PPE occurs around boreal spring both in 2012 and 2013. It is interesting to see a burst of PPE in early 2012, which can also be identified in Figure 10. The spring peak of PPEs leads that of PPEt (Figure 14a). To investigate this further, we compare the time series of SSS and SST contributions to PPE (Figure 15a) with their contributions to meridional density gradient (Figure 15b). If the seasonality of the PPE is related to baroclinic instability (see equation (A(A2b)) of the Appendix A), one would expect to see a seasonal correlation between the PPE and the background meridional density gradient. The latter is a factor of the baroclinic conversion term in the middle of the right hand side of equation (A(A2b)) in the Appendix A. From Figure 15a, the estimated lead time of the boreal-spring peak of PPEs over that of PPEt is 35 days in 2012 and 28 days in 2013. The boreal-spring peak of the SSS contribution to meridional density gradient also leads that of the SST contribution during this season (Figure 15b). The correlation between the time series of the SSS (SST) contributions to PPE and SSS (SST) contributions to meridional density gradient is 0.73 (0.54), both being significant at the 95% confidence level. The values of the correlation are moderate probably because we are only analyzing the meridional component of the density gradient, and there is some dependence on the scale over which the meridional gradient is estimated (we used a central difference scheme on the 1/3° grid). Nevertheless, they illustrate the overall relation between the PPE and the magnitude of the meridional density gradient.

At the PIRATA mooring location of 0°, 23°W, the relative contributions by PPEt, PPEs, and PPEts to PPE are similar to those at 1°N, 16°W (Table 1). Ignoring the effects of SSS would also underestimate PPE by approximately three times. This is consistent with the finding of *Grodsky et al.* [2005] who found that including salinity effect increased the estimated baroclinic energy conversion rate by a factor of three at this location. This agreement suggests that TIW-related surface PPE is primarily contributed by baroclinic energy conversion in this region.

For the location near the Congo River outflow (5°S, 8°E), PPEs is twice as large as PPEt while PPEts is close to PPEt. Ignoring SSS effect would underestimate PPE by a factor of four, indicating a more important role of SSS in this region than in the central equatorial Atlantic. On average, the Congo River discharge has a maximum around November–December and a secondary peak around April–May [*Materia et al.*, 2012]. The

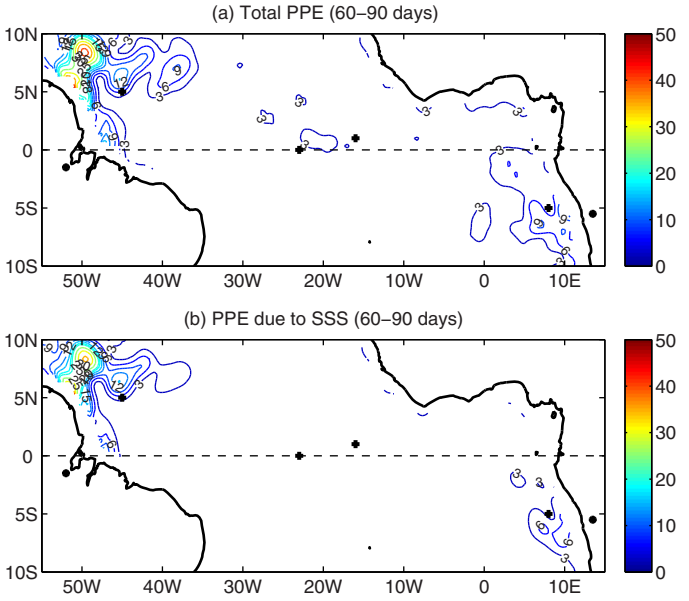

Figure 16. (a) The time mean of the total PPE, and (b) the contribution by SSSA for the 60–90 day signals. The unit is Joule·m^{-3}. The locations of the crosses are the same as those in Figure 13.

PPE time series near the Congo River outflow region (Figure 14c) likewise has a peak in November–December and has a secondary peak before mid-year both for 2012 and 2013. While the peak in late 2012 was primarily contributed by SSS, that in late 2013 was contributed by SST, SSS, and SST-SSS covariability. The SSS contribution in late 2013 is about four times smaller than that in late 2012. In terms of SSSA, the magnitude in late 2012 is smaller than that of 2013 by a factor of two. An analysis of the Congo River discharge data obtained from http://www.ore-hybam.org indicates that the maximum discharge of the Congo River in late 2013 is smaller than that in 2012 by 4% (not shown). While this is not inconsistent with the smaller effect of SSS on PPE in 2012, it is not clear if the 4% reduction in Congo River discharge is sufficient to affect the meridional SSS gradient to reduce the SSSA by a factor of two. The potential effect of precipitation on SSSA on the 20–50 day time scales needs to be investigated.

At the location near the NBC retroflection region (5°N, 48°W), PPEs has a dominant contribution to PPE. Not accounting for SSS effect would underestimate PPE by a factor of ten (Table 1). The PPE peak occurred in July 2012 and 2013 (Figure 14d), which is consistent with the timing of maximum discharge of the Amazon River [*Lentz*, 1995] and the NBC retroflection [*Johns et al*., 1990].

The discussion so far has emphasized the 20–50 day period band where TIWs exhibit significant variability. However, *Johns et al*. [1998] reported that the variability in the NBC retroflection region was dominated by fluctuations with periods near 25–40 days and 60–90 days, with the former being more surface trapped. Therefore, we also examined the PPE for the 60–90 day signals. Figures 16a and 16b are equivalent to Figures 13a and 13c but for the 60–90 day signals. The largest PPE for this period band occurs near the NBC retroflection and the Congo River outflow regions. The total effects of SSS account for approximately 90% of the contribution to PPE, with 63–73% due to the direct effect of SSS.

4. Conclusions

More than 2 years of SSS data derived from the Aquarius/SAC-D satellite mission are analyzed along with satellite-derived SST and SSH and in situ salinity data from Argo and the PIRATA array to assess Aquarius' capability to detect TIWs in the tropical Atlantic Ocean and to investigate the effects of SSS on these forms of variability. Aquarius SSS data are able to capture the phase propagation and seasonal variability of the SSS signature related to the Atlantic TIWs. At 1°N where the TIWs are the most energetic in terms of SSS and SST variability, the magnitude of the TIW-related SSS anomalies is $\pm$0.25 psu, which is smaller than their Pacific counterpart by 50%. The averaged westward propagation speed estimated from SSSA, SSTA and SSHA at this latitude is 0.5 m·s^{-1} during the period of the study.

In the central equatorial Atlantic, SSS contribution to the mean meridional density gradient is similar to the SST contribution. It becomes larger (smaller) than the SST contribution in the western (eastern) part of the basin by a factor of 1.5–2. Because of its significant contribution to mean meridional density gradient, SSS plays an important role to TIW-related surface density anomalies and PPE. Its contribution to the latter

comes from both the direct effect of SSS and the indirect effect due to SSS-SST covariability that reenforce the density anomalies. Not accounting for SSS effect would underestimate surface PPE by approximately three times. This is in excellent agreement with *Grodsky et al*. [2005] who found that the inclusion of salinity increases the estimated baroclinic energy conversion rate by a factor of three at the 0°, 23°W PIRATA mooring location. SSS also affects the timing of the seasonal variability of the TIWs. The peak of the PPE in boreal spring due to SSS leads that due to SST by approximately one month.

In the northeast Atlantic near the Amazon outflow and NBC retroflection and in the southeast near the Congo River outflow, SSS effects account for 80–90% of the mean meridional density gradient. As a result, intraseasonal variations of SSS (on time scales of 20–90 days) in these regions have a dominant contribution to surface PPE. The timing of the seasonal peaks of surface PPE in these regions coincide with those of the maximum discharge of the Amazon and Congo Rivers, respectively.

Our study offers a basin-wide perspective for the equatorial Atlantic Ocean and illustrates the important influence of salinity both on the spatial structure and on the seasonal variability of the TIWs. It also provides another demonstration of Aquarius' contribution to improving the understanding of TIWs.

Appendix A : Energy Budget for Fluctuating Flow

The influence of salinity on the TIWs can be considered from the perspective of TIW energetics. Let $\vec{v} = (u\ v,\ w)$ represent the vector velocity with the corresponding zonal, meridional, vertical component, ρ, and p denote potential density and pressure. These fields can be decomposed into the background and perturbation (i.e., the deviation from the background):

$$u=\bar{u}+u',\ v=\bar{v}+v',\ w=w+w',\ \rho=\bar{\rho}+\rho',\ p=\bar{p}+p' \tag{A1}$$

where the overbar and apostrophe represent the time average over a period longer than that of the perturbations (e.g., 50 day running mean in our case) and the deviation from that time average (i.e., the perturbations over 20–50 day time scales). We examined the variability less than 20 days and found them to be very weak. Following *Brooks and Niiler* [1977], the approximate equations that govern the temporal change of the perturbation kinetic energy (PKE) and perturbation potential energy (PPE) averaged over the periods of the perturbation are given by:

$$\frac{1}{2}\rho_o\frac{d}{dt}\left(\overline{u'^2}+\overline{v'^2}\right)=\rho_o\left(-\overline{u'v'}\frac{\partial\overline{u}}{\partial y}-\overline{u'v'}\frac{\partial\overline{v}}{\partial x}-\overline{u'u'}\frac{\partial\overline{u}}{\partial x}-\overline{v'v'}\frac{\partial\overline{v}}{\partial y}\right) \tag{A2a}$$

$$+\rho_o\left(-\overline{u'w'}\frac{\partial\overline{u}}{\partial z}-\overline{v'w'}\frac{\partial\overline{v}}{\partial z}\right)-\nabla\cdot\overline{\vec{v}'p'}-g\overline{w'\rho'} \tag{A2b}$$

$$\frac{1}{2}g\left(\frac{\partial\rho_0}{\partial z}\right)^{-1}\frac{d}{dt}\left(\overline{\rho'^2}\right)=g\left(\frac{\partial\rho_0}{\partial z}\right)^{-1}\left(-\overline{u'\rho'}\frac{\partial\overline{\rho}}{\partial x}-\overline{v'\rho'}\frac{\partial\overline{\rho}}{\partial y}-\overline{w'\rho'}\right) \tag{A3}$$

The four terms on the right-hand side (RHS) of line (A2a) of equation (A2a) represents the conversion between background kinetic energy and PKE through the horizontal Reynolds stresses acting on the horizontal shear of the currents, usually referred to as barotropic (instability) conversion. The first two terms of line (A2b), involving the vertical Reynolds stresses acting on the vertical shear of the currents, are associated with Kelvin-Helmholtz instability. The third term of line (A2b) is the pressure work. In the PPE equation (equation (A3)), the first two terms on the RHS represent the conversion between background available PE and PPE (i.e., baroclinic conversion). The last term of equations (A2) and (A3) couple the two equations together with a common vertical buoyancy flux $\overline{w'\rho'}$, reflecting the conversion between KE and PE. The sign and magnitude of this term due to TIWs are poorly known in large part because there is no measurement of vertical velocity. For this reason, most studies of energetics combined equations (A2) and (A3) to remove this common term [e.g., *Brooks and Niiler*, 1977; *Rossby*, 1987; *Weisberg and Weingartner*, 1988; *Grodsky et al*., 2005]. If $\overline{w'\rho'}$ is small, the temporal changes of PKE and PPE would be primarily associated with barotropic (and Kelvin-Helmholtz) and baroclinic conversions, respectively.

The calculation of baroclinic (and barotropic) conversion requires velocity time series. Mooring measurements of velocity are very limited, basically confined to a few locations at the equator and often with gaps in the time series. There exist surface current products based on satellite altimetry (to obtain the surface

geostrophic velocity) and wind stress estimates from atmospheric analysis or reanalysis (to obtain the wind-driven frictional velocity) for the Aquarius period. An example is the Ocean Surface Current Analysis Real-time (OSCAR) [*Bonjean and Lagerloef*, 2002, http://podaac.jpl.nasa.gov/dataset/OSCAR_L4_OC_third-deg]. The reliability of the estimated surface current near the equator is an issue because of the use of a beta approximation as the geostrophic assumption breaks down. Also, meridional velocities in the OSCAR product near the equator are not as accurate as zonal velocities. Moreover, the fidelity of atmospheric analysis winds (through which the frictional component of the surface velocity is derived) is questionable on TIW time scales because they do not resolve TIWs as scatterometers do [*Wen et al*., 2012]. *Wen et al*. [2012] also found that the coupled assimilation used in generating the NOAA Climate Forecast System Reanalysis (CFSR) product results in an improvement in the representation of the TIW expression in the surface fluxes (including wind stress). Given the challenge of estimating the fluctuations of the surface currents on TIW time scales accurately near the equator (especially for the meridional component), estimating PPE presents an advantage in studying TIW energetics because it does not require velocity information (even though it limits the ability to diagnose the relative contribution of zonal and meridional baroclinic conversion). This is the main motivation for our analysis of PPE in this study.

From equations (A2) and (A3), one can see that salinity can affect TIW energetics through different variables/quantities of the energy budget. Salinity can affect the background horizontal density gradient $\frac{\overline{\partial \rho}}{\partial x}$ and $\frac{\overline{\partial \rho}}{\partial y}$ (with the latter being dominant). It also affects the density anomaly ρ' and thus the horizontal buoyancy flux $\overline{u'\rho'}$ and $\overline{v'\rho'}$. Both of these will influence the baroclinic conversion. The baroclinic conversion changes the PPE, which by itself is proportional to the square of the density anomaly. The vertical buoyancy flux $\overline{w'\rho'}$ is also affected by salinity and regulates the conversion between KE and PE. The discussion of the influence of salinity on the TIWs presented in this paper focuses on the effects of SSS on the background density gradient, density anomaly, and PPE for reasons described above.

Note that the approximate energy equations (A2) and (A3) do not include dissipation and the effects of atmospheric forcing such as the direct generation of KE by wind stress and direct production of surface density anomaly by air-sea heat flux and evaporation-precipitation. Because TIWs are coupled ocean-atmosphere features, there would be some contributions from atmospheric forcing on TIW time scales. However, such contributions might be small compared to the variability purely associated with the oceanic instability because the existence of TIWs are fundamentally due to oceanic instability even though they are modulated by air-sea interaction.

Acknowledgments

This research was carried out in part at the Jet Propulsion Laboratory, California Institute of Technology, under a contract with the National Aeronautics and Space Administration. This is PMEL contribution 4156. The gridded Aquarius data used in this study were provided by Gary Lagerloef (lager@esr.org) and Hsun-Ying Kao (hkao@esr.org) of Earth and Space Research. The links of all other data used in this study were provided in in section 2 "Data" of this paper. We thank Xiaobin Yin of LOCEAN-IPSL for providing the Matlab script and instruction of Radon transform and Seymon Grodsky of University of Maryland for providing the source of the Congo River discharge.

References

Baturin, N. G., and P. P. Niiler (1997), Effects of instability waves in the mixed layer of the equatorial Pacific, *J. Geophys. Res.*, *102*, 27,771–27,793.

Bonjean, F., and G. S. E. Lagerloef (2002), Diagnostic model and analysis of the surface currents in the tropical Pacific Ocean, *J. Phys. Oceanogr.*, *32*, 2938–2954.

Bourlès, B., et al. (2008), The PIRATA Program: History, accomplishments, and future directions. *Bull. Am. Meteorol. Soc.*, *89*, 1111–1125.

Boutin, J., N. Martin, X.-B. Yin, J. Font, N. Reul, and P. Spurgeon (2012), First assessment of SMOS data over open ocean: Part-II-Sea surface salinity, *IEEE Trans. Geosci. Remote Sens.*, *50*, 1662–1675, doi:10.1109/TGRS.2012.2184546.

Boutin, J., N. Martin, G. Reverdin, X. Yin, and F. Gaillard (2013), Sea surface freshening inferred from SMOS and Argo salinity: Impact of rain, *Ocean Sci.*, *9*, 183–192, doi:10.519/os-9-183-2013.

Brooks, I. H., and P. P. Niiler (1977), Energetics of Florida Current, *J. Mar. Res.*, *35*, 163–191.

Caltabiano, A. C. V., I. S. Robinson, and L. P. Pezzi (2005), Multi-year satellite observations of instability waves in the Tropical Atlantic Ocean, *Ocean Sci.*, *1*, 97–112.

Castelão, G. P., W. E. Johns (2011), Sea surface structure of North Brazil Current rings derived from shipboard and moored acoustic Doppler current profiler observations, *J. Geophys. Res.*, *116*, C01010, doi:10.1029/2010JC006575.

Chelton, D. B. (2005), The impact of SST specification on ECMWF surface wind stress fields in the Eastern Tropical Pacific, *J. Clim.*, *18*, 530–550, doi:10.1175/JCLI-3275.1.

Chelton, D. B., F. J. Wentz, C. L. Gentemann, R. A. de Szoeke, and M. G. Schlax (2000), Satellite microwave SST observations of transequatorial tropical instability waves, *Geophys. Res. Lett.*, *27*, 1239–1242, doi:10.1029/1999GL011047.

Chelton, D. B., Esbensen, S. K. Schlax, N. Thum, and M. H. Freilich (2001), Observations of coupling between surface wind stress and sea surface temperature in the eastern tropical Pacific, *J. Clim.*, *14*, 1479–1498.

Dessier, A., and J. R. Donguy (1994), The sea surface salinity in the tropical Atlantic between 10S and 30N-Seasonal and interannual variations (1977–1989), *Deep Sea Res., Part I*, *41*, 81–100.

Evans, W., P. G. Strutton, and F. P. Chavez (2009), Impact of tropical instability waves on nutrient and chlorophyll distributions in the equatorial Pacific, *Deep Sea Res., Part I*, *56*, 178–188.

Farrar, J. T. (2008), Observations of the dispersion characteristics and meridional sea level structure of equatorial waves in the Pacific Ocean, *J. Phys. Oceanogr.*, *38*, 1669–1689, doi:10.1175/2007JPO3890.1.

Farrar, J. T., and T. S. Durland (2012), Wavenumber–frequency spectra of inertia–gravity and mixed Rossby–gravity waves in the equatorial Pacific Ocean, *J. Phys. Oceanogr.*, *42*, 1859–1881, doi:10.1175/JPO-D-11-0235.1.

Feely, R. A., R. Wanninkhof, C. E. Cosca, M. J. McPhaden, R. H. Byrne, F. J. Millero, F. P. Chavez, T. Clayton, D. M. Campbell, and P. P. Murphy (1994), The effect of tropical instability waves on CO_2 species distributions along the equator in the eastern equatorial Pacific during the 1992 ENSO event, *Geophys. Res. Lett.*, *21*, 277–280, doi:10.1029/93GL03212.

Gorgues, T., C. Menkes, O. Aumont, J. Vialard, Y. Dandonneau, and L. Bopp (2005), Biogeochemical impact of tropical instability waves in the equatorial Pacific, *Geophys. Res. Lett.*, *32*, L24615, doi:10.1029/2005GL024110.

Grodsky, A. S., J. A. Carton, C. Provost, J. Servain, J. A. Lorenzzetti, and M. J. McPhaden (2005), Tropical instability waves at 0N, 23W in the Atlantic: A case study using Pilot Research Moored Array in the Tropical Atlantic (PIRATA) mooring data, *J. Geophys. Res.*, *110*, C08010, doi:10.1029/2005JC002941.

Hashizume, H., S. P. Xie, W. T. Liu, and K. Takeuchi (2001), Local and remote atmospheric response to tropical instability waves: A global view from space, *J. Geophys. Res.*, *106*, 10,173–10,185.

Hayes, S. P., M. J. McPhaden, and J. M. Wallace (1989), The influence of sea surface temperature upon surface wind in the eastern equatorial Pacific: Weekly to monthly variability, *J. Clim.*, *2*, 1500–1506.

Jochum, M., and P. Malanotte-Rizzoli (2003), On the generation of North Brazil Current rings. *J. Mar. Res.*, *61*, 147–173, doi:10.1357/002224003322005050.

Jochum, M., and R. Murtugudde (2006), Temperature advection by tropical instability waves, *J. Phys. Oceanogr.*, *36*, 592–605, doi:10.1175/JPO2870.1.

Jochum, M., P. Malanotte-Rizzoli, and A. Busalacchi (2004), Tropical instability waves in the Atlantic Ocean, *Ocean Modell.*, *7*, 145–163.

Johns, W. E., T. N. Lee, F. A. Schott, R. J. Zantopp, and R. H. Evans (1990), The North Brazil Current retroflection – seasonal structure and eddy variability, *J. Geophys. Res.*, *95*, 22,103–22,120, doi:10.1029/JC095iC12p22103.

Johns, W. E., T. N. Lee, R. C. Beardsley, J. Candela, R. Limeburner, and B. Castro (1998), Annual cycle and variability of the North Brazil Current, *J. Phys. Oceanogr.*, *28*, 103–128, doi:10.1175/1520-0485(1998)028<0103:ACAVOT>2.0.CO;2.

Kim, S.-B., T. Lee, and I. Fukumori (2007), Mechanisms controlling the interannual variation of mixed layer temperature averaged over the NINO3 region, *J. Clim.*, *20*, 3822–3843.

Lagerloef, G., et al. (2008), The Aquarius/SAC-D mission-–Designed to Meet the Salinity Remote Sensing Challenge, *Oceanography*, *21*, 68–81.

Lee, T., G. Lagerloef, M. M. Gierach, H.-Y. Kao, S. S. Yueh, and K. Dohan (2012), Aquarius reveals salinity structure of tropical instability waves, *Geophys. Res. Lett.*, *39*, L12610, doi:10.1029/2012GL052232.

Legeckis, R. V. (1977), Long waves in the eastern equatorial ocean, *Science*, *197*, 1177–1181.

Legeckis, R. V., and G. Reverdin (1983), Long waves in the equatorial Atlantic Ocean during 1983, *J. Geophys. Res.*, *92*, 2835–2842, doi:10.1029/94JC01847.

Lentz, S. J. (1995), Seasonal variations in the horizontal structure of the Amazon plume inferred from historical hydrography data, *J. Geophys. Res.*, *100*, 2391–2400.

Liu, W. T., X. Xie, P. S. Polito, S.-P. Xie, and H. Hashizume (2000), Atmospheric manifestation of tropical instability wave observed by QuikSCAT and tropical rain measuring mission, *Geophys. Res. Lett.*, *27*, 2545–2548.

Lumpkin, R., and S. Garzoli (2005), Near-surface circulation in the tropical Atlantic Ocean, *Deep Sea Res., Part I*, *52*, 495–518, doi:10.1016/j.dsr.2004.09.001.

Luther, D. S., and E. S. Johnson (1990), Eddy energetic in the upper equatorial pacific during the Hawaii-to-Tahiti Shuttle Experiment, *J. Phys. Oceanogr.*, *20*, 913–944.

Lyman, J. M., D. B. Chelton, R. A. deSzoeke, and R. M. Samelson (2005), Tropical instability waves as a resonance between equatorial Rossby waves*, *J. Phys. Oceanogr.*, *35*, 232–254, doi:10.1175/JPO-2668.1.

Lyman, J. M., G. C. Johnson, and W. S. Kessler (2007), Distinct 17- and 33-day tropical instability waves in subsurface observations. *J. Phys. Oceanogr.*, *37*, 855–872.

Masina, S., S. G. H. Philander, and A. B. G. Bush (1999), An analysis of tropical instability waves in a numerical model of the Pacific Ocean. 2. Generation and energetics of the waves, *J. Geophys. Res.*, *104*, 29,637–29,661.

Materia, S., S. Gauldi, A. Navarra, et al. (2012), The effect of Congo River freshwater discharge on eastern equatorial Atlantic climate variability, *Clim. Dyn.*, *39*, 2109–2125, doi:10.1007/s00382-012-1514-x.

McCain, C. R., J. R. Christian, S. R. Signorini, M. R. Lewis, I. Asanuma, D. Turk, C. Dupouy-Douchement (2002), Satellite ocean-color observations of the tropical Pacific Ocean, *Deep Sea Res., Part II*, *49*, 2533–2560.

McCreary, J. P., and Z. Yu (1992), Equatorial dynamics in a 2-1/2 layer model, *Prog. Oceanogr.*, *29*, 61–132.

McPhaden, M. J. (1996), Monthly period oscillations in the Pacific North Equatorial Countercurrent, *J. Geophys. Res.*, *101*, 6337–6359, doi:10.1029/95JC03620.

McPhaden, M. J., M. Fieux, and J. Gonella (1984), Meanders observed in the surface currents and hydrography during an equatorial Atlantic transect, *Geophys. Res. Lett.*, *11*, 757–760, doi:10.1029/GL011i008p00757.

Menkes, C., E. R. Christophe, J. G. Vialard, S. C. Kennan, J.-P. Boulanger, G. V. Madec (2006), A modeling study of the impact of tropical instability waves on the heat budget of the eastern equatorial Pacific, *J. Phys. Oceanogr.*, *36*, 847–865, doi:10.1175/JPO2904.1.

Philander, S. G. H. (1978), Instabilities of zonal equatorial currents, Part 2, *J. Geophys. Res.*, *83*, 3679–3682.

Pezzi, L. P., J. Vialard, K. J. Richards, C. Menkes, and D. Anderson (2004), Influence of ocean-atmosphere coupling on the properties of tropical instability waves, *Geophys. Res. Lett.*, *31*, L16306, doi:10.1029/2004GL019995.

Polito, P., and W. T. Liu (2003), Global characterization of Rossby waves at several spectral bands, *J. Geophys. Res.*, *108*(C1), 3018, doi:10.1029/2000JC000607.

Polito, P., and O. T. Sato (2003), Patterns of sea surface height and heat storage associated to intraseasonal Rossby waves in the tropics, *J. Geophys. Res.*, *108*(C12), 3373, doi:10.1029/2002JC001684.

Polito, P., J. Ryan, W. T. Liu, and F. P. Chavez (2001), Oceanic and atmospheric anomalies of tropical instability waves, *Geophys. Res. Lett.*, *2233-2236*, doi:10.1029/2000GL012400.

Qiao, L., and R. H. Weisberg (1995), Tropical instability wave kinematics: Observations from the Tropical Instability Wave Experiment, *J. Phys. Oceanogr.*, *100*, 8677–8693.

Qiao, L., and R. H. Weisberg (1998), Tropical instability wave energetics: Observations from the Tropical Instability Wave Experiment, *J. Phys. Oceanogr.*, *28*, 345–360.

Reynolds, R. W., T. M. Smith, C. Liu, D. B. Chelton, K. S. Casey, and M. G. Schlax (2007), Daily high-resolution-blended analyses for sea surface temperature, *J. Clim.*, *20*, 5473–5496.

Richardson, P. L., and G. Reverdin (1987), Seasonal cycle of velocity in the Atlantic North Equatorial Countercurrent as measured by surface drift3ers, current meters, and ship drifts, *J. Geophys. Res.*, *92*, 3691–3708, doi:10.1029/JC092iC04p03691.

Rossby, T. (1987), On the energetics of the Gulf Stream at 73W, *J. Mar. Res.*, *45*, 59–82.

Strutton, P. G., J. P. Ryan, and F. P. Chavez (2001), Enhanced chlorophyll associated with tropical instability waves in the equatorial Pacific, *Geophys. Res. Lett.*, *28*, 2005–2008, doi:10.1029/2000GL012166.

Urbano, D. F., R. A. F. De Almeida, and P. Nobre (2008), Equatorial undercurrent and North Equatorial Countercurrent at 38°W: A new perspective from direct velocity data, *J. Geophys. Res.*, *113*, C04041, doi:10.1029/2007JC004215.

von Schuckmann, K., P. Brandt, and C. Eden (2008), Generation of tropical instability waves in the Atlantic Ocean, *J. Geophys. Res.*, *113*, C08034, doi:10.1029/2007JC004712.

Weisberg, R. H., and T. J. Weingartner (1988), Instability waves in the equatorial Atlantic Ocean, *J. Phys. Oceanogr.*, *18*, 1641–1657.

Wen, C., Y. Xue, and A. Kumar (2012), Tropical instability waves simulated in the NCEP climate forecast system reanalysis, *J. Clim.*, *25*, 6409–6425.

Xie, S. P., M. Ishiwatari, H. Hashizume, and K. Takeuchi (1998), Coupled ocean-atmospheric waves on the equatorial front, *Geophys. Res. Lett.*, *25*, 3863–3966.

Yoder, J. A., S. G. Ackleson, and R. T. Barber (1994), A line in the sea, *Nature*, *371*, 689–692.

Yu, J.-Y., and W. T. Liu (2003), Seasonal and interannual variations of northern and southern tropical instability waves and their coupling with the atmosphere, *Geophys. Res. Lett.*, *30*(14), 1735, doi:10.1029/2003GL017176.